

# Internal resistance and polarization dynamics of lithium-ion batteries upon internal shorting



Daniel J. Noelle<sup>a</sup>, Meng Wang<sup>b</sup>, Anh V. Le<sup>b</sup>, Yang Shi<sup>a</sup>, Yu Qiao<sup>a,b,\*</sup>

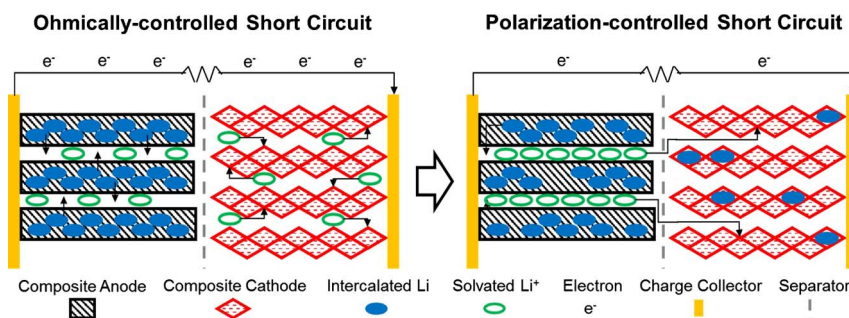
<sup>a</sup> Program of Materials Science and Engineering, University of California – San Diego, La Jolla, CA 92093, USA

<sup>b</sup> Department of Structural Engineering, University of California – San Diego, La Jolla, CA 92093, USA

## HIGHLIGHTS

- Understanding resistive dynamics informs thermal runaway mitigation strategies.
- Internal resistance at high discharge rates is dynamic and nonlinear.
- Electrical resistances dictate short circuit current in crucial first seconds.
- Rapid polarization depletes lithium-ion presence in electrolyte of cathode region.
- Ionic resistances throttle short circuit heating rates upon cell polarization.

## GRAPHICAL ABSTRACT



## ARTICLE INFO

### Keywords:

Lithium-ion battery  
Thermal runaway  
Safety  
Short circuit  
Resistance  
Polarization

## ABSTRACT

Internal resistance and temperature measurements are made for LIR2450 format LiCoO<sub>2</sub>/graphite 120 mA h coin cells upon abusive discharge conditions. The dynamic contributions of electrical and ionic resistances to joule heat generation are investigated in the earliest stages of battery failure. It is shown that while ohmic, primarily electrical resistances initially dictate the joule heating rates, polarization, primarily ionic resistances become dominant as time progresses. Ionic conductivity and resistance of LiPF<sub>6</sub> salt in ethylene carbonate/ethyl methyl carbonate solvent are examined through concurrent concentration, viscosity, and temperature measurements to elucidate the intricacies of electrolyte polarization. Comparative analysis suggests that upon polarization at high discharge rates, resistance is concentrated in the electrolyte within the cathode region due to rapid depletion of lithium-ions available to facilitate charge transfer. Expected consequences are corroborated in external shorting and nail penetration experiments. The findings are used to predict how a cell would respond if electrical or ionic resistances are exacerbated upon shorting, so as to identify effective thermal runaway mitigation strategies.

## 1. Introduction

Lithium-ion batteries (LIB) carry safety risks inherent to their energy-dense chemistries and flammable components, which are of notable concern due to complications associated with thermal runaway [1,2]. LIB safety is particularly important for cells and modules in electric vehicles, which are prone to physical abuse in collision events

[3,4]. When short circuit joule heating causes temperature to accrue to a critical point between 110 °C and 150 °C in high capacity cells [5], cascading exothermic electrochemical reactions and chemical decompositions compound to accelerate temperature increase, which can reach more than 500 °C in a matter of seconds [6]. These conditions lead to electrolyte ignition and possibly unit explosion [7]. Reported battery failures have gained the attention of both academic and

\* Corresponding author at: 9500 Gilman Drive, MC 0085, University of California – San Diego, La Jolla, CA 92093-0085, USA.  
E-mail address: [yqiao@ucsd.edu](mailto:yqiao@ucsd.edu) (Y. Qiao).

| Nomenclature    |  |                  |  |
|-----------------|--|------------------|--|
| $A$             | ionic conductivity relation proportionality constant ( $S\cdot Pa\cdot s\cdot m^2\cdot mol^{-1}\cdot K^{-1}$ ) | $t$              | time (s)   |
| $c_p$           | effective system heat capacity ( $J\cdot g^{-1}\cdot K^{-1}$ )   | $t_{ini}$        | initial time of heat dissipation frequency coefficient measurement interval (s)      |
| $C$             | lithium-ion concentration of electrolyte ( $mol\cdot m^{-3}$ )   | $T$              | temperature (K)  |
| $C_0$           | lithium-ion concentration of unpolarized electrolyte ( $mol\cdot m^{-3}$ )                                     | $T_0$            | ambient temperature (K)  |
| $\bar{C}_i$     | average lithium-ion concentration of electrolyte in select region ( $mol\cdot m^{-3}$ )                        | $V_{emf}$        | electromotive force (V)  |
| $E_A$           | activation energy of electrolyte viscosity ( $J\cdot mol^{-1}$ )   | $V_t$            | terminal voltage (V)   |
| $E_{A,1}$       | first parameter defining activation energy of electrolyte viscosity ( $J\cdot mol^{-1}$ )                      | <i>Greek</i>     |  |
| $E_{A,2}$       | second parameter defining activation energy of electrolyte viscosity ( $m^3\cdot mol^{-1}$ )                   | $\delta_i$       | thickness of select region (m)   |
| $h_{dis}^*$     | heat dissipation frequency coefficient (Hz)  | $\varepsilon$    | permittivity of electrolyte solvent  |
| $I_x$           | current rate for select discharge type (A)   | $\varepsilon_1$  | first parameter defining permittivity of electrolyte solvent                         |
| $m$             | cell system mass (g)   | $\varepsilon_2$  | second parameter defining permittivity of electrolyte solvent ( $K^{-1}$ )           |
| $\dot{q}_{dis}$ | rate of heat dissipation (W)   | $\mu$            | viscosity of electrolyte (Pa·s)  |
| $\dot{q}_{gen}$ | rate of heat generation (W)  | $\mu^*$          | reference viscosity of electrolyte (Pa·s)  |
| $\dot{q}_{net}$ | net rate of heating/cooling (W)  | $\mu_1^*$        | first parameter defining reference viscosity of electrolyte (Pa·s)                   |
| $Q$             | charged current capacity (A·h)   | $\mu_2^*$        | second parameter defining reference viscosity of electrolyte ( $m^3\cdot mol^{-1}$ ) |
| $r_{p,i}$       | specific resistance of polarized electrolyte in select region ( $\Omega$ )                                     | $\sigma$         | ionic conductivity of electrolyte ( $S\cdot m^{-1}$ )                                |
| $R$             | ideal gas constant ( $J\cdot mol^{-1}\cdot K^{-1}$ )   | <i>Subscribe</i> |  |
| $R_{elec}$      | resistance of electrolyte ( $\Omega$ )   | $i$              | select region, = a, c, or s  |
| $R_{ext}$       | external shorting resistance ( $\Omega$ )  | $x$              | select discharge type, = app or sc   |
| $R_{int}$       | internal resistance ( $\Omega$ )   | $a$              | anode  |
| $R_o$           | ohmic resistance ( $\Omega$ )  | $c$              | cathode  |
| $R_p$           | polarization resistance ( $\Omega$ )   | $s$              | separator  |
| $R_{p,i}$       | polarization resistance contribution of electrolyte in select region ( $\Omega$ )                              | $app$            | applied  |
|                 |  | $sc$             | short circuit  |

industrial researchers to identify the causes, and to understand the progression of events that beset thermal runaway. These objectives serve to minimize risk by informing responsible day-to-day operation and aiding in development of effective failsafe technologies [8,9].

Risks associated with joule heating and electrochemical degradation during normal operation are well controlled in electric vehicles. Intelligent battery management system (BMS) algorithms [10,11] coupled with efficient battery thermal management system (BTMS) designs [12–14] ensure that the temperature throughout the battery pack is maintained in a suitable temperature range below 40 °C at all times. Additionally, the state of health is constantly monitored by the onboard computer system [15,16], which identifies any hazardous conditions to be addressed [17]. As a result, thermal runaway is of minor concern under normal operating conditions. However, vehicles may still catch fire in accidents if the battery pack is physically damaged. Collisions can cause the formation of short circuit discharge pathways which the BMS cannot control, nor the BTMS can manage. The battery pack is afforded extensive protection to minimize the possibility and extent of damage, but it is acknowledged that unmitigated damage may still take place in certain circumstances [4,9].

The exothermic decomposition events encompassing thermal runaway have been extensively studied [5,6]. By understanding the nature of how heat generation accelerates as temperature rises, thermal runaway mitigation technologies can be incorporated within the cells and modules to halt temperature increase, and specialized battery materials can be employed to tolerate excessive temperature [9]. Most failsafe features are thermally triggered, taking effect at a specific temperature above the normal LIB operating range (> 80 °C), but below the critical acceleration point (< 150 °C) [8,18–27]. They typically involve phase change materials or positive temperature coefficient materials that slow down temperature increase upon activation. Such technologies are

capable of handling short circuits of moderate power, but may fail to manage severe short circuits in large-format LIB cells. In the event of a vehicle crash, it is preferable that LIBs have inherent failsafe features that take effect in the joule heating regime, irrespective of temperature and immediately upon shorting, but work in this area is uncommon [28–31].

In severe short circuit scenarios, joule heating dynamics are dictated by the internal resistance of the LIB cell [32–34]. The sum of the resistive contributions from a multitude of internal components limit the discharge current and consequent temperature increase [35,36], which in turn alters the resistance of those components in various ways. The resistive influence of fast kinetic processes manifest rapidly. Those processes include charge transfer between the electrode and electrolyte, as well as electron movement through the composite electrode and across current collector interfaces [37]. Resistive effects of slower processes, like charge-carrying ion diffusion in electrolyte and solid-state ion diffusion within active electrode particles, become apparent on longer timescales [38]. Initially, the resistive kinetic contributions are more significant, such that the short circuit is ohmically-controlled, but as time progresses and resistive diffusion phenomena become dominant, the aggressive discharge transitions to be polarization-controlled. Surveying those resistive phenomena in the diverse network of sensitive materials organized in unwieldy and inaccessible arrangements within an LIB cell is difficult, particularly when engaged in fast, dynamic electrochemical and chemical processes [34,39].

Many experimental studies concerning severe short circuit failure have been performed on large-format LIB cells [34–36,40–44]. These tests produce fast temperature increases that often result in fire or explosion. Such study is critical to understanding the dangerous heat transfer propagation characteristics within cells and through modules. However, they do not offer systematic information concerning the

fundamental joule heating dynamics that seed the energy to trigger all the other undesirable energetic phenomena.

Large-format LIB cells impose challenges to in-situ determination of the resistive contributions from individual components, as well as the progression of events which might alter their significance to the resultant current, as short circuit discharge proceeds. Their short circuit dynamics are aggressive to the point where measurements of joule heating are convoluted by other exothermic decomposition phenomena and nonuniform conduction [33]. Information on the dynamics of how internal resistance changes during the shorting process to define the joule heating rate in the early stages of shorting are limited to computational simulations, which are challenging to verify experimentally [32,33,35,36]. Development of experimental methods to examine the resistive dynamics of LIB cells under shorting conditions is critical to informing LIB safety protocols and improving cell safety features [33,36].

The goal of this study is to gain a better understanding of how the internal resistance dynamics of LIB cells influence the initial stages and progression of a short circuit failure induced by severe mechanical abuse. Using experimental methods designed specifically to study the joule heating regime, the nature and influence of those phenomena are analyzed. A framework is discussed for the identification and development of effective thermal runaway mitigation strategies addressing short circuit discharge at its earliest stages, which bridge the gap between primary protection structures and thermally triggered failsafe features.

## 2. Experimental procedure and data processing

### 2.1. Reference cell system

Internal resistance and temperature measurements were taken during abusive discharge and short circuit experiments using LIR2450 format LiCoO<sub>2</sub>/graphite 120 mA h coin cells, obtained from Xiamen TOB New Energy Technology. The LIR2450 coin cells were chosen as the reference system specifically to investigate the joule heating regime. When severely abused, their current capacity was sufficient to produce consequential cell temperature increase up to 100 °C. Such temperature accrual was measured over a resolute timescale on the order of minutes, without reaching the critical temperature range where decomposition events characteristic of thermal runaway might occur. In this manner, joule heating data measurements were not convoluted by other exothermic phenomena. Furthermore, the simple geometry of the rigid 304 stainless steel case structure of LIR2450 cell ensured secure electrical and thermal contact within, even during nail penetration experiments. The large mass contribution of the thermally conductive cell case aided in heat generation measurement, which allowed for an assumption of isothermal character when measuring the temperature externally, despite the fact that most heat was generated from its internal components where the temperature might be slightly different.

### 2.2. Direct current internal resistance testing

Internal resistance ( $R_{int}$ ) dynamics under healthy and abusive applied constant current ( $I_{app}$ ) discharge conditions were determined through direct current internal resistance (DCIR) analysis using a Neware BTS3000-5V6A Battery Analyzer. The electromotive force ( $V_{emf}$ ) and terminal voltage ( $V_t$ ) were compared to differentiate the ohmic, primarily electrical resistance and polarization, primarily ionic resistance contributions. The ohmic resistance ( $R_o$ ) was characterized by the instantaneous potential drop upon resistor application, while polarization resistance ( $R_p$ ) collectively described all additional overpotential manifestations as time ( $t$ ) progressed. DCIR measurements were taken for cells subject to constant current discharge pulses with rates ranging from 0.2 C (24 mA) to 10 C (1200 mA). Cell temperature ( $T$ ) was simultaneously monitored using a type-K gage-40

thermocouple affixed to the center of the cell case on the cathode side by polyimide tape. Data were sampled once every second.

$$R_{int}(t) = R_o + R_p(t) \quad (1)$$

The LIR2450 cells were preconditioned by cycling twice between 3.0 V and 4.2 V at a constant applied current rate of 0.1 C. The electromotive force was measured by tracking the terminal voltage from 4.2 V during the second discharge cycle, as a function of charged current capacity ( $Q$ ) [45]:

$$V_{emf}(Q) = V_t(Q, I_{app} = 0.1 \text{ C}) \quad (2)$$

The obtained data were used to assess how the electromotive force changes with the state of charge (SOC) [46]:

$$Q(t) = Q(t=0) - I_{app}t \quad (3)$$

DCIR tests were performed by applying constant current discharge pulses at various applied current rates on 2-min intervals. For each test, the cell was charged at 0.1 C to the starting potential of 4.0 V and allowed to rest for 1 h, ensuring stable open circuit voltage prior to discharge. The ohmic resistance was calculated from the initial potential drop based on the first voltage measurement made upon discharge initiation, sampled at 1 s after external resistor application [16,47–49]:

$$R_o = \frac{V_{emf}(t=0) - V_t(t=1s)}{I_{app}} \quad (4)$$

The dynamic polarization resistance was measured as discharge progressed with respect to terminal voltage deviations from the electromotive force, accounting for the ohmic resistance bias:

$$R_p(t) = \frac{V_{emf}(Q(t)) - V_t(t)}{I_{app}} - R_o \quad (5)$$

Ohmic resistance was assumed constant for the testing duration while polarization resistance was differentiated.

The 4.0 V starting potential of the DCIR measurement was selected in recognizing the influence of SOC on charge transfer resistance and other kinetic processes. Those kinetic phenomena are notably more resistive when a cell is fully charged or discharged, but relatively constant between 30% and 80% SOC [38,48]. Furthermore, the electromotive force was measured at a rather slow discharge rate, such that the ohmic overpotential bias is low and any minor polarization disturbances incurred would have ample time to develop and reach steady-state by 4.0 V, where it is compared with the terminal voltage [49]. The 2-min measurement period was selected to capture expected non-linearities in polarization resistance and produce consequential joule heat generation at abusive discharge rates for analysis over resolute temperature and time scales, while remaining within the described SOC range for the entire duration of all DCIR experiments.

### 2.3. External shorting and nail penetration testing

The short circuit responses of the LIB cells were tested externally via constant resistance discharge in a similar manner to the constant current tests, as well as internally via nail penetration. In both cases, the LIB cells were preconditioned by cycling twice between 3.0 V and 4.2 V at a rate of 0.1 C, tracking the electromotive force in terms of charged current capacity during the second discharge cycle. They were then fully charged to 4.2 V and allowed to rest for 1 h prior to short circuit initiation.

External shorting was performed using the BTS3000-5V6A Battery Analyzer, in which the positive and negative terminals of the cell were connected by a 110 mΩ resistor ( $R_{ext}$ ) for a 2-min period. The short circuit current response ( $I_{sc}$ ) was measured directly using the analyzer.

Internal shorting was induced by driving a stainless steel nail (3.8 mm diameter, 50 mm long) through the cell at its center point using a drill press. In the absence of directly measured terminal voltage

and current data, the short circuit current response was calculated indirectly. Without an external resistor to accept energy upon discharge, all current moves through the internal components of the cell, which act as the only resistors in the circuit. In this event, all stored energy is discharged as joule heat. The power of the discharge is driven by the entire electromotive force of the cell and the short circuit current allowed by its internal resistance, which dictates the rate of joule heat generation ( $\dot{q}_{\text{gen}}$ ). Hence, the rate of joule heat generation can be estimated through analysis of the dynamic temperature response and compared with the electromotive force, in order to determine the short circuit current [6,42]:

$$I_{\text{sc}}(t) = \frac{\dot{q}_{\text{gen}}(t)}{V_{\text{emf}}(Q(t))} \quad (6)$$

Changes to electromotive force as a function of temperature were not considered in this calculation.

Prior to shorting via nail penetration, the charged cells were secured to a 12 mm thick polyurethane base holder using masking tape. The assembly was fastened to the drill press in order to facilitate quick nail penetration through the center point, without any lateral movement or large cell deformation. A type-K gage-40 thermocouple was affixed 6 mm from the center of the cell on the cathode side and temperature response was measured over a 20-min period. Details of the joule heat generation rate calculation are given in Section 2.4.

The ohmic resistance and dynamic polarization resistance responses of the cells were determined by comparing short circuit currents with the electromotive force, accounting for bias of the applied resistor in the external shorting scenario [42,49]:

$$R_o = \frac{V_{\text{emf}}(t=0)}{I_{\text{sc}}(t=1\text{s})} \quad (7)$$

$$R_p(t) = \frac{V_{\text{emf}}(Q(t))}{I_{\text{sc}}(t)} - R_o - R_{\text{ext}} \quad (8)$$

The depth of discharge was tracked with reference to the short circuit current, so as to distinguish how the electromotive force changes as time progresses [46]:

$$Q(t) = Q(t=0) - \int_{t=0}^t I_{\text{sc}}(t) dt \quad (9)$$

Data were sampled for the short circuit experiments once every second.

The fully charged, 4.2 V starting potential for the short circuit tests was selected to produce the largest temperature signal possible, for analysis of the most severe scenarios. The anticipated degree of polarization is well in excess of any minor polarization disturbances incurred in the 0.1 C electromotive force measurements. Moreover, the SOC undergoes large variations upon shorting.

#### 2.4. Determining heat transfer characteristics

A convective heat transfer relation was employed to correlate joule heat to the temperature response, taking into consideration the contributions of the heat generation rate and the heat dissipation rate ( $\dot{q}_{\text{dis}}$ ) to the net heating/cooling rate ( $\dot{q}_{\text{net}}$ ) of the cell [50,51]:

$$\dot{q}_{\text{net}}(t) = \dot{q}_{\text{gen}}(t) - \dot{q}_{\text{dis}}(t) \quad (10)$$

The net heating/cooling rate reflected in the rate at which the cell temperature changes, is related to the cell mass ( $m$ ) and the effective system heat capacity ( $c_p$ ):

$$\dot{q}_{\text{net}}(t) = mc_p \frac{dT(t)}{dt} \quad (11)$$

The heat generation rate is coupled to the measured current ( $I_x$  representing  $I_{\text{app}}$  or  $I_{\text{sc}}$  where appropriate) and the internal resistance [6,42]:

$$\dot{q}_{\text{gen}}(t) = I_x(t)^2 R_{\text{int}}(t) \quad (12)$$

The heat dissipation rate is governed by the magnitude of the difference between cell temperature and ambient temperature ( $T_0$ ), as well as a heat dissipation frequency coefficient ( $h_{\text{dis}}^*$ ) that reflects the thermal conductivity and external orientation of the system:

$$\dot{q}_{\text{dis}}(t) = mc_p h_{\text{dis}}^* [T(t) - T_0] \quad (13)$$

Entropic and radiative heat transfer effects were not considered in this relation.

The heat dissipation frequency coefficient was determined irrespective of the system mass and effective system heat capacity by tracking the cell temperature upon cooling over a 2-min interval after discharge, when all heat generation was presumed to have stopped [51]:

$$h_{\text{dis}}^*(\dot{q}_{\text{gen}} = 0) = -\ln \left[ \frac{T(t) - T_0}{T(t_{\text{ini}}) - T_0} \right] / [t - t_{\text{ini}}] \quad (14)$$

The initial time of the measurement interval ( $t_{\text{ini}}$ ) for the DCIR testing scenarios was 1 min after induced discharge had ceased. This interval was chosen to avoid any interference from heat of mixing effects within the electrolyte as it recovered from polarization during the initial relaxation period [39,51], but while measured temperature was sufficiently different from the ambient temperature to produce a resolute, dynamic cooling signal.

After the cell mass was identified using a Fischer Scientific Analytical Balance and the heat dissipation frequency coefficient was known, the effective system heat capacity could be deduced. The value was determined based on the proportionality between the total joule heat generated by the end of the DCIR tests, as calculated from the applied current rates and internal resistances, versus the consequent temperature accrue ment associated with the joule heating phenomenon, accounting for the heat dissipated from the system mass over the duration of the discharge timeframe:

$$c_p = \left[ \int_{t=0\text{s}}^{t=120\text{s}} I_{\text{app}}^2 R_{\text{int}}(t) dt \right] / \left[ \int_{t=0\text{s}}^{t=120\text{s}} m \left[ \frac{dT(t)}{dt} + h_{\text{dis}}^*(T(t) - T_0) \right] dt \right] \quad (15)$$

The 6 C, 8 C, and 10 C DCIR scenarios were selected to assess these heat transfer parameters, and the average determined coefficient values were applied for all DCIR data analyses. The lower discharge rate DCIR scenarios were not considered for heat transfer parameter determination, due to the insufficient temperature accrue ment.

The system mass, effective system heat capacity, and heat dissipation frequency coefficient were different for the nail penetration test. They were recalculated to account for the added mass and altered geometry introduced by the protruding nail, as well as the insulation provided by the polyurethane base holder. The mass of nail was measured using the balance and considered with the cell mass. Furthermore, the effective system heat capacity, as measured from the DCIR tests, was adjusted to account for the additional heat capacity of the 304 stainless steel nail, based on the known specific heat of 304 stainless steel [52]. The 2-min measurement interval of the heat dissipation frequency coefficient began 10 min after the nail penetration was performed. At the selected point in time, all stored energy had been expended and any heat generation had stopped, but a high temperature differential for parameter assessment remained as the cell cooled during the evaluation period.

The testing results used to determine the heat dissipation frequency coefficient and the effective system heat capacity are shown in Section 4.1. The determined values of all coefficients used in the heat transfer analyses are summarized in Table 1.

#### 2.5. Electrolyte conductivity and viscosity measurement

Electrolyte conductivity measurements for LiPF<sub>6</sub> salt in ethylene

**Table 1**  
Heat transfer measurement parameters.

| Discharge test   | $m$ (g) | $c_p$ (J·g <sup>-1</sup> ·K <sup>-1</sup> ) | $h_{dis}^*$ (Hz) |
|------------------|---------|---|------------------|
| DCIR             | 4.86    | 1.4   | 0.0055           |
| Nail penetration | 7.66    | 1.07  | 0.0029           |

carbonate (EC)/ethyl methyl carbonate (EMC) solvent solutions were made using a Yoke DDS-307A Conductivity Meter at 23 °C, with the salt concentrations ranging from 0.1 M and 2.37 M. Viscosity dependence on LiPF<sub>6</sub> salt concentration and temperature was determined by testing electrolyte solutions of varied salt concentrations for temperatures ranging from 23 °C and 63 °C, using an NDJ-9S Digital Rotary Viscometer with a #0 rotor low viscosity adapter. Temperature control was achieved by using a water bath on a hot plate. The electrolyte solutions were prepared by adjusting the molarity of BASF Selectilyte LP50 1 M LiPF<sub>6</sub> EC:EMC (1:1 w:w) electrolyte either by dilution with additional EC (Sigma Aldrich #E26258) and EMC (Sigma Aldrich #754935) mixed in 1:1 mass ratio, or dissolution of additional LiPF<sub>6</sub> salt (Sigma Aldrich #201146).

### 3. Model development and calibration

#### 3.1. Modeling electrolyte conductivity

Ionic conductivity ( $\sigma$ ) collectively captures the availability and the mobility of the charge-carrying ions in electrolyte solution. The charge carrier availability is determined by the lithium-ion concentration ( $C$ ) and the ion mobility is dictated by the permittivity ( $\epsilon$ ) of solvent and the diffusivity of solvated ions. Valøen and Reimers showed that diffusivity varies strongly with concentration and temperature, expressing that appropriate understanding of how they affect transport dynamics is particularly important when predicting electrolyte performance at high currents, when a cell is prone to consequential self-heating [53]. Recognizing how particles diffuse through liquids at low Reynolds numbers with respect to the Stokes-Einstein relation, considering ion diffusivity dynamics in terms of temperature and fluid viscosity ( $\mu$ ) may assist in anticipating ionic conductivity changes as battery cell temperature increases [54].

Viscosity of carbonate based electrolytes can increase drastically with salt concentration, producing thick, relatively low-conductivity fluids [55,56]. In high molarity solutions this becomes relevant as a cell polarizes and concentration imbalances are induced across the characteristic length of the transport pathway [32,57]. Considering these factors relevant to a cell operating under stress, conductivity is predicted as:

$$\sigma(C,T) = A \left[ \frac{CT\epsilon(T)}{\mu(C,T)} \right] \quad (16)$$

where a constant of proportionality ( $A$ ) describes the magnitude of the electrolyte conductivity.

As viscosity has Arrhenius-type dependence on temperature [56], it is written as:

$$\mu(C,T) = \mu^*(C,T_0) \exp \left[ \frac{E_A(C)}{R} \left( \frac{1}{T} - \frac{1}{T_0} \right) \right] \quad (17)$$

where the reference viscosity ( $\mu^*$ ) and the activation energy ( $E_A$ ) are functions of salt concentration. For a given concentration, the reference viscosity is tabulated at the ambient temperature of 23 °C and the activation energy relative to the ideal gas constant ( $R$ ) is determined based on a series of viscosity measurements at 9 temperatures for each of 7 tested concentrations (Fig. 1). Both the reference viscosity and the activation energy are determined to have exponential dependence on concentration:

$$\mu^*(C,T_0) = \mu_1^* \exp(\mu_2^* C) \quad (18)$$

$$E_A(C) = E_{A,1} \exp(E_{A,2} C) \quad (19)$$

where the reported magnitudes of the variables defining exponential dependence ( $\mu_1^*$ ,  $\mu_2^*$ ,  $E_{A,1}$ , and  $E_{A,2}$ ) are determined empirically.

A linear dependence of permittivity on temperature for the EC:EMC (1:1 w:w) solvent has been previously reported by Hall et al. [58] as:

$$\epsilon(T) = \epsilon_1 - \epsilon_2 T \quad (20)$$

where the reported magnitudes of the variables defining linear dependence ( $\epsilon_1$  and  $\epsilon_2$ ) are applied directly to the ionic conductivity model.

The measured conductivity values are used in calibrating the constant of proportionality so as to provide the best fit relating concentration, temperature, permittivity, and viscosity to the modelled conductivity for the LiPF<sub>6</sub> EC:EMC (1:1 w:w) electrolyte system. The measurements also serve to validate the model at 23 °C (Fig. 2). The values of all coefficients for the conductivity model are summarized in Table 2.

#### 3.2. Relating electrolyte and polarization resistance

The determined ionic conductivity model is applied between concentrations of 0 M and 2 M up to 80 °C, and is used to construct a relative electrolyte resistance model for comparison with measured polarization resistances in DCIR and short circuit testing (Fig. 3). The relative electrolyte resistance ( $R_{elec}$ ) for a given concentration and temperature is related to the nominal resistance of the 1 M LiPF<sub>6</sub> initial unpolarized concentration ( $C_0$ ) at 23 °C as:

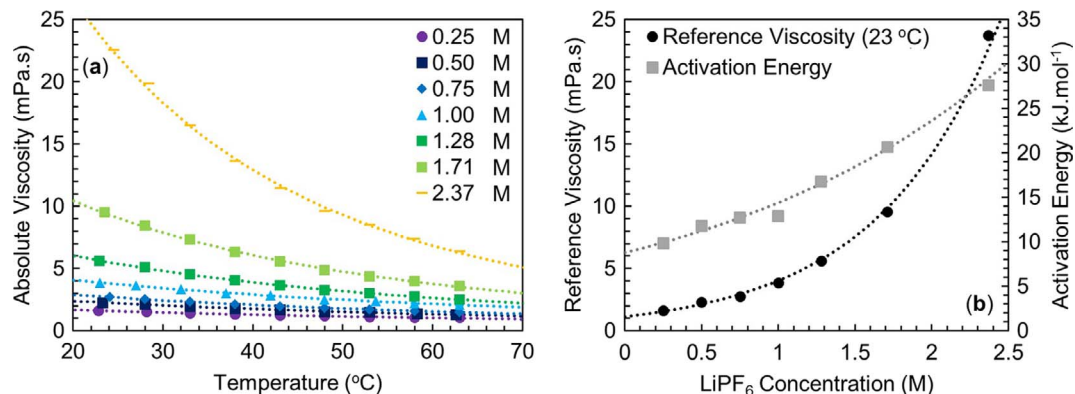


**Fig. 1.** (a) Measured viscosity ( $\mu$ ) of LiPF<sub>6</sub> EC:EMC (1:1 w:w) electrolyte as a function of temperature ( $T$ ) for salt concentrations ( $C$ ) from 0.25 M to 2.37 M. (b) Fitted Arrhenius-type viscosity parameters ( $\mu^*$  and  $E_A$ ) as functions of the salt concentration.

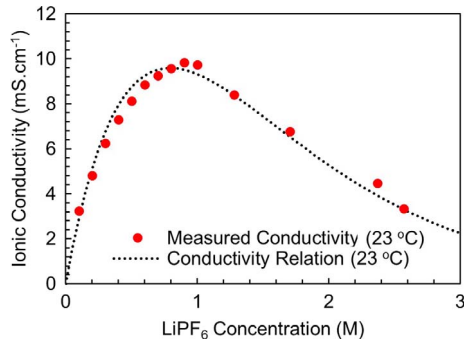


Fig. 2. Measured and modeled ionic conductivity ( $\sigma$ ) of LiPF<sub>6</sub> EC:EMC (1:1 w:w) electrolyte as a function of the salt concentration ( $C$ ) at 23 °C ( $T_0$ ).

$$\frac{R_{\text{elec}}(C, T)}{R_{\text{elec}}(C_0, T_0)} = \frac{\sigma(C_0, T_0)}{\sigma(C, T)} \quad (21)$$

### 3.3. Ion polarization

The dynamic local average lithium-ion concentrations in electrolyte within the cathode ( $\bar{C}_c$ ), separator ( $\bar{C}_s$ ), and anode regions ( $\bar{C}_a$ ) are determined for the DCIR and short circuit scenarios, considering the measured polarization resistance and cell temperature dynamics. The sum of the resistance contributions from the polarized electrolyte in the three regions ( $R_{p,c}$ ,  $R_{p,s}$ , and  $R_{p,a}$ ) must equal the polarization resistance measured upon discharge:

$$R_p(t) = \sum_{i=c,s,a} R_{p,i}(\bar{C}_i, T, t) \quad (22)$$

As electrolyte resistance is proportional to the length which a charge-carrier travels and all three regions exhibit similar porosity, the specific resistances within each region ( $r_{p,c}$ ,  $r_{p,s}$ , and  $r_{p,a}$ ) are weighted in terms of their individual component thicknesses ( $\delta_c$ ,  $\delta_s$ , and  $\delta_a$ ), to determine their contributions to the total polarization resistance:

$$R_{p,i}(\bar{C}_i, T, t) = \left[ \frac{\delta_i}{\delta_c + \delta_s + \delta_a} \right] r_{p,i}(\bar{C}_i, T, t) \quad (23)$$

The average concentrations in the electrolyte within the cathode and the anode regions are related to each other, such that lithium-ion species conservation is retained:

$$\delta_c \bar{C}_c(t) + \delta_a \bar{C}_a(t) = [\delta_c + \delta_a] C_0 \quad (24)$$

The concentration in the electrolyte within the separator region is considered to be constant:

$$\bar{C}_s(t) = C_0 \quad (25)$$

The measured resistance profile of the 0.2 C DCIR test is taken as a reference, representing the nominal electrolyte resistance of an unchanging, 1 M lithium-ion concentration in all three regions at 23 °C for the entire 2-min testing duration.

For each of the discharge tests, the polarized local average electrolyte concentrations and their corresponding resistance contributions are determined simultaneously using a shooting method. The lithium-ion concentration of electrolyte within the cathode region is varied on an interval of 0.001 M between 0.001 M and 1.0 M at the temperature of the examined moment in time, while the respective ion concentration within the anode region is varied accordingly to maintain the ion

species balance. Each set of concentrations are cross-referenced with the formulated relative electrolyte resistance model described in Section 3.2. The specific resistances of all three regions are determined based on proportionality to the nominal electrolyte reference:

$$\frac{r_{p,i}(\bar{C}_i, T, t)}{R_p(I_{\text{app}} = 0.2C, t)} = \frac{R_{\text{elec}}(\bar{C}_i, T)}{R_{\text{elec}}(C_0, T_0)} \quad (26)$$

The resistance contributions of the polarized electrolyte in each region, weighted by their individual component thicknesses, are totaled and compared with the measured polarization data from the DCIR or short circuit test at the moment of interest. The set of local average concentrations that produce the resistance data which matches the experimentally measured polarization resistance total is identified.

The micrometer measured individual component thicknesses of disassembled cells are summarized in Table 3.

## 4. Discussion

### 4.1. Results of direct current internal resistance testing

While ohmic resistance is relatively constant regardless of the discharge rate ( $R_o = [0.52\Omega, 0.72\Omega]$ ), the polarization resistance is variable, becoming increasingly significant as the discharge current increases ( $R_p(t = 2 \text{ min}) = [0.59\Omega, 3.82\Omega]$ ) (Fig. 4). Only minor increases in polarization resistance are realized relative to the established reference in the low current discharge regime (1.0 C and below). This is especially true in the first minute following resistor application, where differences in polarization resistance are effectively indistinguishable from the reference. However, notable increases in resistance are observed in the elevated current discharge regime (above 1.0 C). The magnitude becomes larger and the rate of polarization becomes faster as the discharge rate increases.

Unlike in the low current discharge regime, elevated discharge current pulses and internal resistance inefficiencies lead to consequential temperature accrual. The rate at which the measured cell temperature returns towards ambience following the high current DCIR and nail penetration tests shows the frequency of heat dissipation (Fig. 5). Considering the joule heat generation rate in terms of applied current and measured resistance dynamics, the effective system heat capacity of the DCIR tested cell systems are determined. The average heat transfer parameter values used in the convective heat transfer model show good agreement with the measured temperature data (Fig. 6).

The ratio between the DCIR polarization resistance measurements and the nominal unpolarized electrolyte resistance profile is cross-referenced with the relative electrolyte resistance model developed for LiPF<sub>6</sub> based in EC:EMC (1:1 w:w) solvent, considering the recorded temperature response. The comparison suggests the degree to which average lithium-ion concentration of the electrolyte within the cathode and anode regions deviates from the initial uniform 1 M concentration as cell polarization proceeds.

### 4.2. Low current discharge regime

Model comparison indicates notable deviations from the initial concentration as polarization occurs in the electrolyte within the cathode and anode regions at low current discharge rates, despite only minor increases in polarization resistance relative to the unpolarized

Table 2

Conductivity relation coefficients for LiPF<sub>6</sub> EC:EMC (1:1 w:w) electrolyte and reference parameters for relative electrolyte resistance.

| $\mu_1^*$ (mPa·s) | $\mu_2^*$ (M <sup>-1</sup> ) | $E_{A,1}$ (J·mol <sup>-1</sup> ) | $E_{A,2}$ (M <sup>-1</sup> ) | $\epsilon_1$ | $\epsilon_2$ (K <sup>-1</sup> ) | $C_0$ (M) | $T_0$ (K) | $A$ (mS·mPa·s·cm <sup>-1</sup> ·M <sup>-1</sup> ·K <sup>-1</sup> ) |
|-------------------|------------------------------|----------------------------------|------------------------------|--------------|---------------------------------|-----------|-----------|--|
| 1.1415            | 1.2605                       | 8784.5                           | 0.4849                       | 82.61        | 0.1645                          | 1         | 296.15    | 0.003737   |

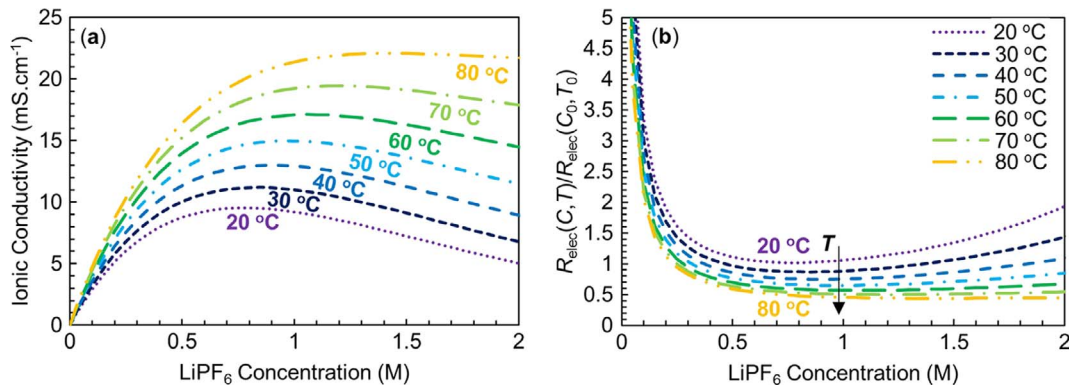


Fig. 3. (a) Modeled ionic conductivity ( $\sigma$ ) of LiPF<sub>6</sub> EC:EMC (1:1 w:w) electrolyte with respect to the salt concentration ( $C$ ) and the temperature ( $T$ ). (b) Corresponding modeled electrolyte resistance ( $R_{elec}$ ) relative to the nominal 1 M LiPF<sub>6</sub> reference concentration ( $C_0$ ) at 23 °C ( $T_0$ ).

**Table 3**  
Thicknesses of composite cathode, separator, and composite anode.

| $\delta_c$ ( $\mu\text{m}$ ) | $\delta_s$ ( $\mu\text{m}$ ) | $\delta_a$ ( $\mu\text{m}$ ) |
|------------------------------|------------------------------|------------------------------|
| 70                           | 20                           | 77.5                         |

electrolyte reference. As charge-carrying lithium-ions are uptaken from the electrolyte by the cathode, lithium-ions are simultaneously deposited into the electrolyte by the anode. Increasing lithium-ion concentration in the electrolyte within the anode region renders the solution more viscous, curbing ion mobility, which results in polarization resistance increase. Decreasing lithium-ion concentration in the electrolyte within the cathode region also contributes to the resistance increases due to decreased availability to facilitate charge transfer, but

consequent reduction in electrolyte viscosity makes the resistive contribution from the cathode region less pronounced. While of the same order of magnitude, ion imbalances in the electrolyte within the anode region has the greatest influence on polarization impedance in the low current discharge regime. Together, resistive contributions from the electrolyte within the cathode and anode regions are no more significant than the ohmic resistance.

#### 4.3. Elevated current discharge regime

Drastic increases in polarization resistance occur at elevated discharge rates as rapid, significant deviations from the initial unpolarized electrolyte concentration take place in both the cathode and anode regions of the LIB cell. Upon polarization at rates of 6.0 C and above, the lithium-ion concentration in the electrolyte within the cathode

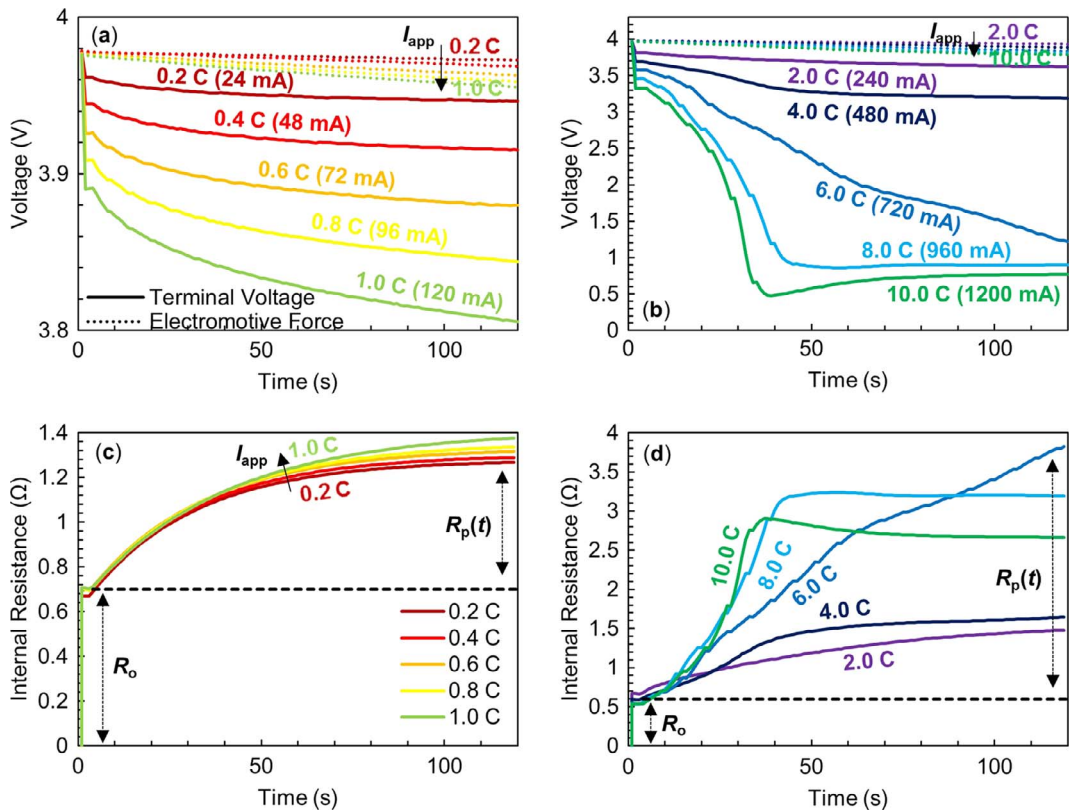


Fig. 4. (a) LIR2450 cell DCIR terminal voltage ( $V_i$ ) and electromotive force ( $V_{emf}$ ) responses for low applied current discharge rates ( $I_{app}$ ) up to 1.0 C and (b) elevated applied current discharge rates of 2.0 C to 10.0 C. (c) Corresponding ohmic resistances ( $R_o$ ) and dynamic polarization resistances ( $R_p$ ) for low current discharge rates and (d) elevated current discharge rates measured over time ( $t$ ).

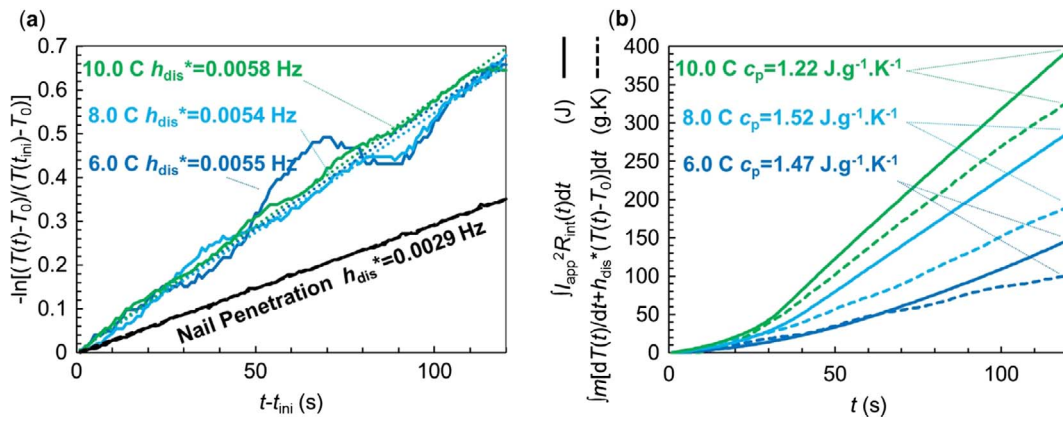


Fig. 5. (a) Heat dissipation frequency coefficients ( $h_{dis}^*$ ) denoting the magnitude of the slope for the linear fitted curves, determined following DCIR and nail penetration tests as cell temperature ( $T$ ) cooled towards ambient temperature ( $T_0$ ) over time ( $t$ ), beginning at the predetermined evaluation time ( $t_{ini}$ ). (b) System heat capacities ( $c_p$ ) denoting the ratio between joule heat generated versus the product of cell mass ( $m$ ) and theoretical temperature accrued without heat dissipation upon DCIR current termination, evaluated in terms of applied current ( $I_{app}$ ), internal resistance ( $R_{int}$ ), measured cell temperature, ambient temperature, heat dissipation frequency coefficient, and time. Relevant numerical relations and evaluating methods are enumerated in Section 2.4.

region is just 2% of its initial value after 2 min, which corresponds with a significant increase in concentration within the anode region. Unlike at low currents where this phenomenon would raise the viscosity in the electrolyte within the anode region, the consequent increase in cell temperature curbs the thickening effect. The lithium-ions tend to maintain a relatively high mobility and the conductive electrolyte within the anode region does not contribute notably to the cell

resistance. Instead, the imbalance of lithium-ions in electrolyte within the cathode region incurs the most significant contribution to polarization resistance and total internal resistance increases, due to the scarcity of charge-carrying ions within that locality.

Discharging at 10 C, the process of polarization occurs over about 35 s, at which time local average ion concentrations stabilize. Prior to polarization, during the first few seconds following resistor application,

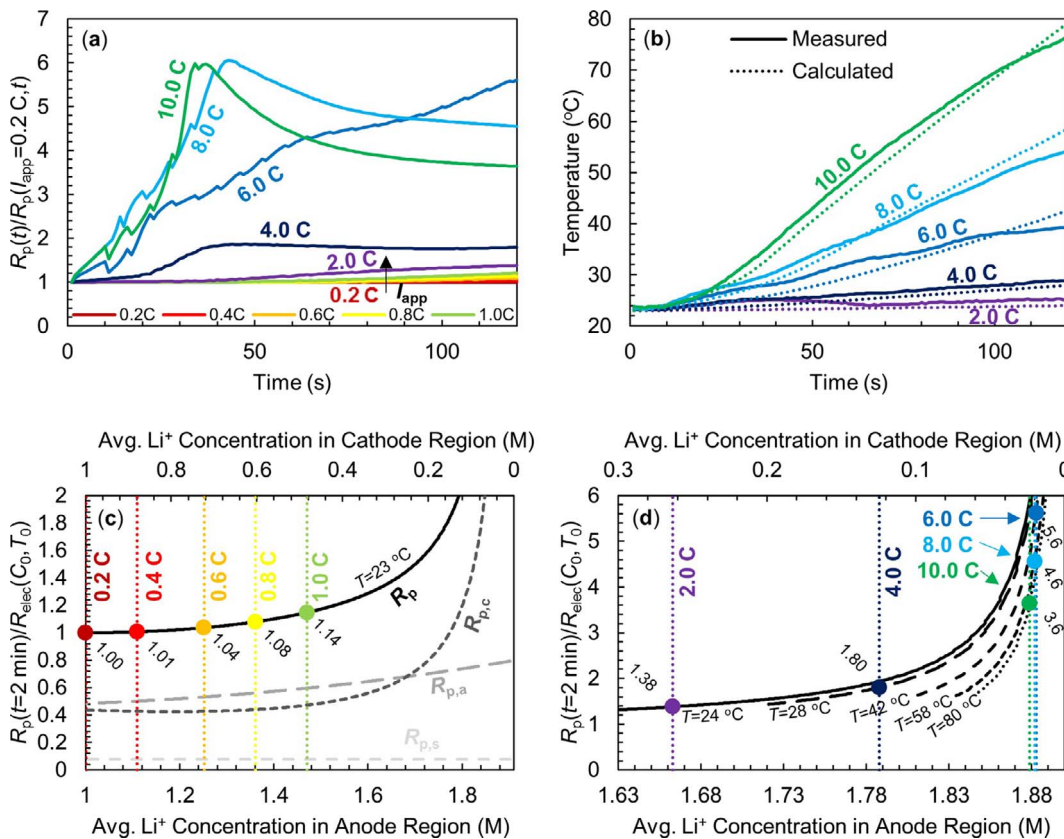


Fig. 6. (a) DCIR dynamic polarization resistance responses ( $R_p$ ) of LIR2450 cells at low and elevated applied current discharge rates ( $I_{app}$ ), relative to the assumed 0.2 C unpolarized 1 M electrolyte reference ( $C_0$ ) profile. (b) Corresponding measured cell temperature ( $T$ ) and calculated cell temperature responses based on the measured DCIR joule heating and heat dissipation rates, using experimentally determined heat transfer parameters applied to the convective heat transfer model described in Section 2.4. (c) Local average lithium-ion concentrations in the electrolyte within the cathode ( $\bar{C}_c$ ) and anode ( $\bar{C}_a$ ) regions at the end of the 2-min DCIR tests for low current discharge rates at 23 °C ( $T_0$ ), showing resistance contributions of the polarized electrolyte within cathode ( $R_{p,c}$ ), anode ( $R_{p,a}$ ), and separator ( $R_{p,s}$ ) regions. (d) Local average lithium-ion concentrations in the electrolyte within the cathode and anode regions at the end of the 2-min DCIR tests for elevated current discharge rates at their final calculated temperatures, determined by the method described in Section 3.3.

the ohmic contributions account for almost the entirety of the measured internal resistance. However, upon polarization, the resistive contributions of the electrolyte within the cathode region accounts for more than 90% of the polarization resistance and more than 70% of the total internal resistance (Fig. 7).

While the ultimate magnitude of the concentration imbalance does not further increase beyond 6.0 C, the rate of polarization becomes quicker, as does the rate of temperature increase. These phenomena are responsible for the nonlinearities of the internal resistance dynamics at elevated discharge rates.

#### 4.4. Function and limitations of this interpretation

This study is designed to identify the ohmic and polarization resistance dynamics of LIB cells under abusive discharge conditions using simple experimental methods in order to better inform thermal runaway mitigation strategies addressing the joule heating regime. Ohmic resistances are primarily electrical in nature, while polarization resistances are primarily ionic; but a multitude of complex phenomena contribute to both and their combined influences under extreme conditions are difficult to accurately predict. The combined contributions of all phenomena that manifest as either ohmic or polarization resistances are collectively captured in the DCIR measurements. Further analysis serves to describe the nature of the polarization, which is significant under abusive discharge conditions. The experimental design choices are made specifically to examine individual elements.

Ohmic resistance is assumed to be constant for the duration of the DCIR tests, but charge transfer resistance, which is a major contributing factor, varies with SOC [38]. To minimize any associated error, the tests are started from about 70% SOC and discharged to a minimum of about 40% SOC in the most aggressive DCIR scenario. Within this SOC range, charge transfer resistance is relatively constant so that polarization resistance can be differentiated from the ohmic contribution [48].

The DCIR response of the 0.2 C applied current test over the duration of the 2-min examination period is selected to represent an unchanging 1 M ion concentration in all three regions, and LiPF<sub>6</sub> salt concentration in EC:EMC (1:1 w:w) solvent represents lithium-ion concentration within the cell. These assumptions are necessary to establish a reference for comparison to ascertain information about ion imbalances upon cell polarization. Arora et al. [57] reported through their computer simulations that when a LiMn<sub>2</sub>O<sub>4</sub>/graphite, 1 M LiPF<sub>6</sub> EC:DMC (2:1 v:v) cell system is subjected to 0.16 C discharge, an average concentration greater than 0.95 M is maintained in the electrolyte within the cathode region after 3 min. Furthermore, deviations of local average concentrations from the initial 1 M unity indicated by the analysis are well beyond that of any bias introduced by using the 0.2 C testing reference.

Small increases in polarization resistance suggest large deviations from the initial concentration in the low current regime. The formulated electrolyte resistance model is quite sensitive for concentrations between 0.5 M and 1.45 M, which introduces a degree of uncertainty as to the accuracy of the local average concentration values at low discharge rates. However, the model provides much better resolution outside of this concentration range and the analysis well captures the ion imbalances at elevated current discharge rates, relevant for short circuit considerations.

This experimental analysis is carried out to identify local average ion concentrations. It does not account for local gradients in the individual cathode, separator, or anode regions. Such dynamics may be important, specifically in the electrolyte within the anode region which thickens exponentially with concentration [32,57]. Concentrations greater than the indicated average may accrue near the anode current collector, which could have a consequential contribution to internal resistance. However, as discussed previously, temperature accrual tends to negate concentration induced viscosity increases, and the resistive contribution of the electrolyte in the cathode region at elevated rates is overwhelming.

The polarization resistance analysis does not consider resistive contributions from solid-state ion diffusion in the active materials. The time constant characteristic of ion diffusional impedance development within the electrolyte is on the order of one to ten seconds [38,53], whereas the time constant for solid-state ion diffusional impedance is on the order of several tens to a couple hundred seconds [37,49]. Solid-state diffusional impedance contributes to the resistance measured at the end of the 2-min DCIR tests to a relatively minor degree, which influences the concentration determinations. Sustained discharge at high rates might also cause particle or interfacial cracking, which could exacerbate resistance as time progresses. However, the polarization resistance increases at high discharge rates occurring in the first tens of seconds over the timescale characterized by the electrolyte diffusional impedance time constant result from ion reallocation across the characteristic length of the transport pathway, and are retained through the duration of the tests.

At high discharge rates, measured internal resistances quickly increase, resulting in consequential joule heating. Through this experimental analysis, it is shown that this is primarily a result of ion depletion from the electrolyte in the cathode region. The models used to make this determination have limitations, and although the experiments are carefully designed with those limitations in mind, a degree of error persists as a result of the collective sum of assumptions required to perform the analyses. Nonetheless, the experimental data and analyses are valuable to the discussion of resistance and polarization dynamics under extreme discharge conditions, and is critical to the study on short circuit joule heating dynamics and thermal runaway mitigation

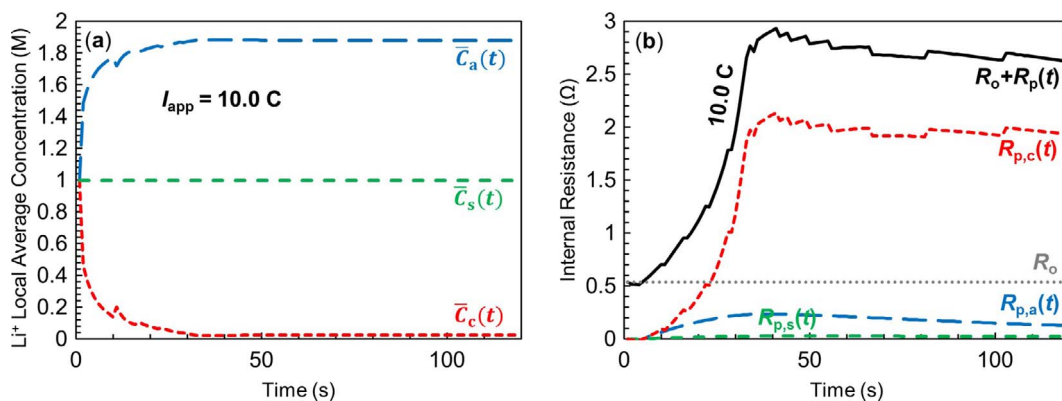


Fig. 7. (a) Local average lithium-ion concentrations in the cathode ( $\bar{c}_c$ ), anode ( $\bar{c}_a$ ), and separator ( $\bar{c}_s$ ) regions for a LIR2450 cell discharged at 10.0 C applied current rate ( $I_{app}$ ), as a function of time ( $t$ ). (b) Ohmic resistance ( $R_o$ ), dynamic polarization resistance contributions from the individual regions ( $R_{p,c}$ ,  $R_{p,a}$ , and  $R_{p,s}$ ), and total polarization resistance ( $R_p$ ) influences to the measured internal impedance, determined by the method described in Section 3.3.

strategies.

#### 4.5. External shorting and nail penetration tests

Unlike during a controlled constant current discharge, where increasing internal resistance and polarization dynamics exacerbate heat generation, internal resistance is discharge rate limiting in short circuit scenarios. Initially dictated by low, ohmic resistances, a short circuit discharge current is expected to be highest at the moment when the short is initiated and decrease as internal polarization proceeds. Heating dynamics proportionally reflect the magnitude of the current, so the LIB cell should respond initially at its maximum possible heating rate and subsequently reduce to a lower rate.

As expected, the measured current and heat generation responses initially peak at their maximum rates. External shorting initially results in a 50 C discharge current and nail penetration results in an 80 C discharge current, both extending a duration of about 3 s. Over the next 10–15 s, discharge rates decrease to and stabilize at about 20 C and 10 C for external shorting and nail penetration, respectively (Fig. 8). When subjected to dynamic ion allocation analysis, the model comparison indicates a rapid depletion of lithium-ions in electrolyte within the cathode region, settling at 1–3% of the initial uniform concentration after the first 3 s. The rapid uptake of nearly all the lithium-ions results in immediate polarization of the cell. Continued discharge thereafter requires that ions traverse longer distances from the concentrated electrolyte within the anode region to allow for further charge transfer, throttling the short circuit current rate. A depiction of this phenomenon is illustrated in the Graphical Abstract.

The electrically-controlled, capacitive discharge peak occurring during the first 3 s reflects 5–7% of the total current capacity of the cell. These values align with the quantity of lithium-ions that occupy the electrolyte within the cathode region prior to initiation of the short circuit. Subsequent discharge of the remaining 93–95% current capacity is ionically-controlled by the resistance of the ion scarce electrolyte within the cathode region. Differences in the magnitude of the capacitive heating rate and subsequent polarization resistance increase for the different modes of shorting are attributed to the different electrical shorting resistances, which result in variable compounding temperature and discharge rate dynamics. Computational simulations of Zavalis et al. [32] suggest similar heating rate and polarization dynamics for a  $\text{LiNi}_{0.8}\text{Co}_{0.15}\text{Al}_{0.05}\text{O}_2/\text{graphite}$ , 1.2 M  $\text{LiPF}_6$  EC:EMC (3:7 w:w) cell system subjected to severe short circuit scenarios.

#### 4.6. Implications for thermal runaway mitigation

While cells are designed to have low operational impedance to maximize their rate capability, charge efficiency, and discharge

efficiency, raising internal resistance in response to the formation of a short circuit connection is critical to halting temperature increase in the joule heating regime, prior to the onset of cascading exothermic decomposition events. The investigation performed to elucidate joule heating, resistance, and polarization dynamics provides guidance on how to identify thermal runaway mitigation strategies relevant to various heating features and timeframes.

According to the experimental and modeling results, targeting and imparting excess electrical resistances is critical to decreasing the magnitude of the powerful capacitive discharge feature demonstrated in the initial seconds following short circuit initiation. This is especially important for high capacity cells in which rapid discharge of 5–7% current capacity may be sufficient to raise temperature to the critical point where thermal runaway accelerates. The timescale of the electrical impedance increase must be fast. Minimizing capacitive discharge heating also helps dampen and delay subsequent conductive contributions incurred by temperature accrual. Electrical resistances contribute relatively little to overall impedance after the capacitive energy has been expended, and are less relevant once the electrolyte has polarized.

Given the immediacy of the capacitive discharge, safety features should be mechanically activated or inherent to the structure of the electrically conductive components. The current collectors and the conductive carbon composite additives are reasonable targets to address this feature, as they provide the least electrically resistive pathways for charge to move between electrodes. Mitigation strategies worthy of investigation include: modification of current collectors as to strategically weaken them, promoting separation of damaged locations from undamaged locations to minimize electrical contact area in an impact event [28]; manipulating conductive carbon morphology to embrittle the electrodes so they easily break apart, limiting electrical contact within the composites when crushed [29]; decreasing conductive carbon loading in the cathode to reduce excessive electrical conductivity that is unneeded to meet functional rate capability requirements; increasing composite electrode thickness to increase electron transport length as well as reduce the possibility of low resistance contact with the counter electrode's current collector [34,35]; to name a few.

Exacerbating ionic resistances is important to halting the continued discharge upon polarization. While polarized-electrolyte-controlled discharge is notably slower than the ohmically-controlled discharge, this regime represents more than 90% of the total current capacity for a fully charged LIB cell. Given sufficient charged current capacity, this ion-transport-dependent feature of short circuit discharge would heat a higher capacity cell to the critical acceleration temperature of thermal runaway, if the electron-transport-dependent feature does not. The timescale for ionic impedance increase is slightly less constrained than

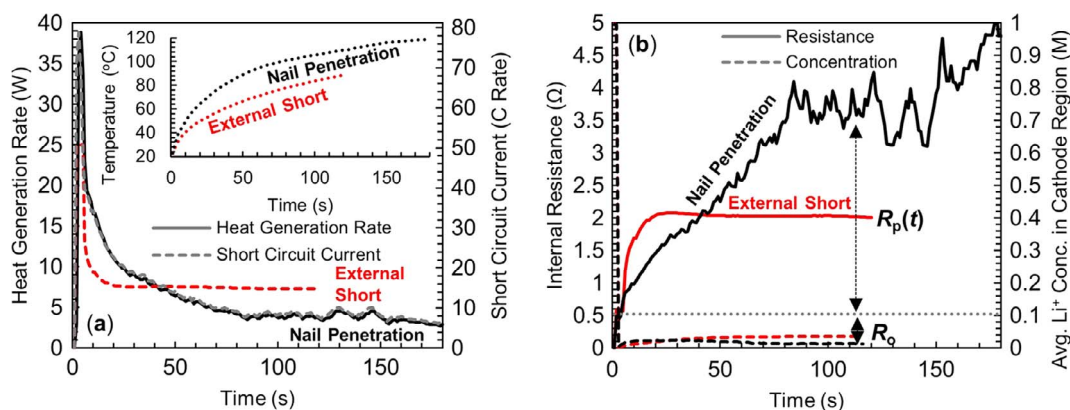


Fig. 8. (a) Heat generation rate ( $\dot{q}_{\text{gen}}$ ), discharge current ( $I_{\text{sc}}$ ), and cell temperature ( $T$ ) responses to external shorting and nail penetration testing of fully charged LIR2450 cells. (b) Corresponding ohmic ( $R_0$ ) and polarization resistances ( $R_p$ ) applied to the experimentally derived relative electrolyte resistance comparison model for  $\text{LiPF}_6$  in EC:EMC (1:1 w:w) solvent, showing rapid depletion of lithium-ion concentration in the electrolyte within the cathode region ( $\bar{C}_c$ ) upon abuse, obtained through the procedures described in Sections 2.3 and 3.3.

electrical impedance increases, but faster responses are still desirable to throttle the continued heat generation as temperature rises. Ionic resistances incur the most significant contributions to internal resistance upon polarization, and they limit the discharge rate for the major duration of the shorting response.

Considering the electrolyte conductivity model helps to identify different methods for manipulating the electrolyte to exacerbate polarization resistance, in order to curb or stop continued joule heating after the capacitive discharge. Given the extreme degree to which concentration is imbalanced upon polarization, it would seem rather difficult to manipulate it further, but forcibly altering the permittivity or viscosity could be viable mitigation approaches. The ion diffusional resistance in electrolyte could be manipulated by: implanting encapsulated poisons within the electrodes or separator, which produce low or zero permittivity regions upon rupture [30]; shear-thickening electrolyte additives, which increase viscosity immediately upon impact prior to temperature increase [31]; less porous anode composites, which restrict ion motion upon polarization; etc.

It is envisioned that with improved understanding of how joule heating proceeds, as well as the significance and nature of the different ohmically-controlled and polarization-controlled discharge features, new techniques may be developed to address short circuit discharge at its earliest stages.

#### 4.7. Significance of abuse responsive impedance increases

The predicted increases in electrically-controlled and ionically-controlled resistances immediately in response to short circuit initiation are shown for the LIR2450 cell system examined upon nail penetration (Fig. 9). Even increasing the resistance twofold ( $2R_o$  and  $2R_p(t)$ ) is consequential to the heating rate and temperature responses. Increasing ohmic resistance has major influence in the first 3 s, and increasing polarization resistance has a greater degree of influence once the capacitive energy has discharged. The different influences of the electrical and ionic resistive modes are apparent when comparing fivefold increases of ohmic resistances ( $5R_o$ ) and polarization resistances ( $5R_p(t)$ )

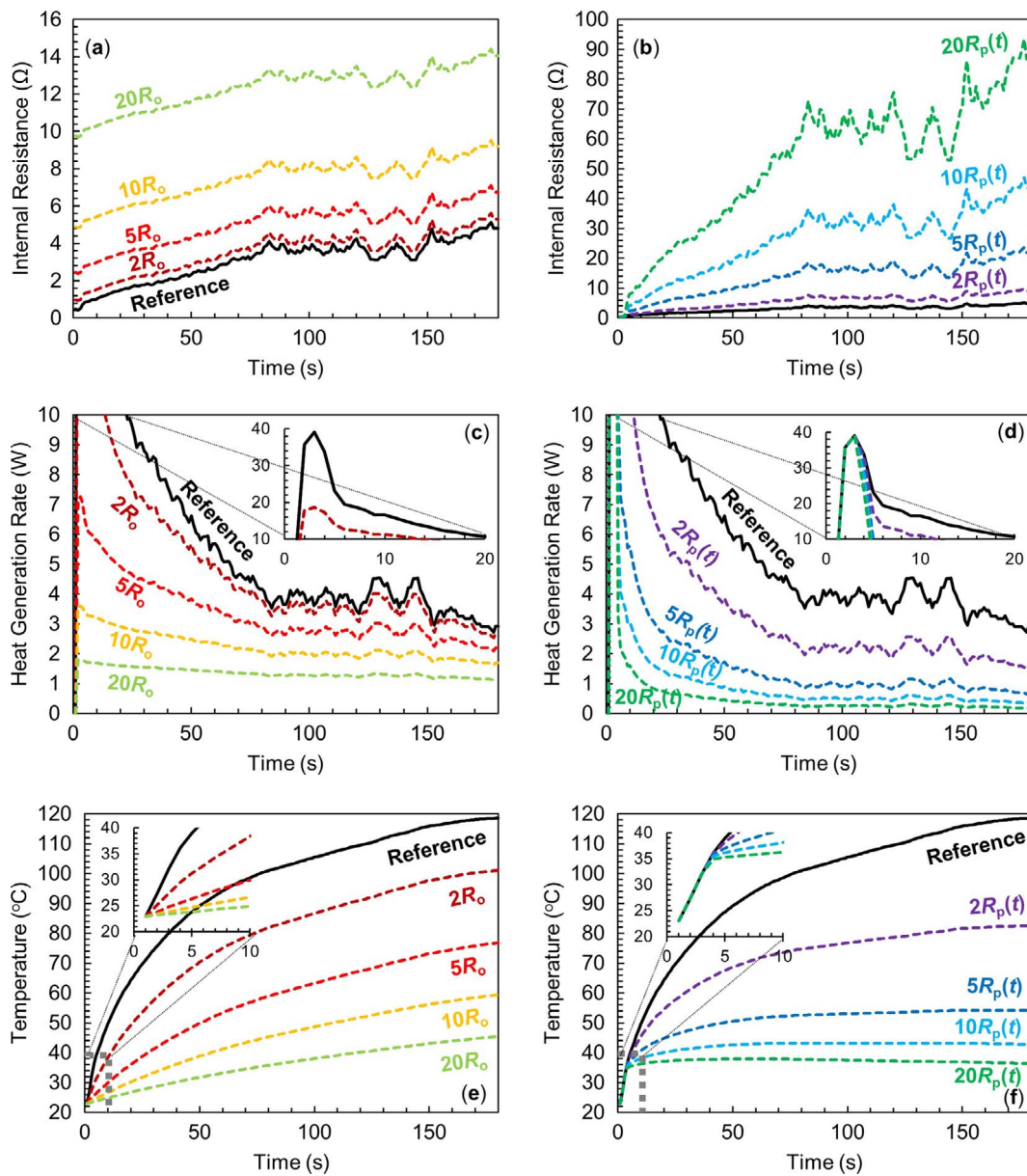


Fig. 9. Predicted internal impedance, heat generation rate ( $\dot{q}_{gen}$ ), and cell temperature ( $T$ ) responses of LIR2450 cells upon nail penetration, subjected to: (a, c, e) increased ohmic resistances or (b, d, f) increased polarization resistances by twofold ( $2R_o$ ,  $2R_p(t)$ ), fivefold ( $5R_o$ ,  $5R_p(t)$ ), tenfold ( $10R_o$ ,  $10R_p(t)$ ), and twentyfold ( $20R_o$ ,  $20R_p(t)$ ) relative to the measured reference response.

independently. While the relative temperature increase is 10 °C less after 3 s in the ohmic increase scenario due to notable suppression of heating associated with capacitive discharge, relative temperature increase is 22 °C less after 3 min for the polarization increase scenario, as the magnitude of the resistance increase is higher for the greater duration of the shorting event.

Heat generation rate in the first 3 s following shorting initiation is inversely proportional to the ohmic resistance increase. In all examined cases, the magnitude of increase in polarization resistance supersedes and continues to grow beyond a proportional increase in ohmic resistance, as the dominant resistive force within 8 s of short circuit initiation. Hence, increasing ion transport resistance would be more effective in throttling the ultimate accrued temperature, but may offer relatively little benefit in the important first few seconds after the connection is formed. That is not to say electrical resistance increases do not have influence after the capacitive discharge energy has subsided. Ten-fold to twenty-fold increases in electrical resistances ( $10R_o$  to  $20R_o$ ) can curb the rate of temperature increase to manageable levels without additionally increasing ionic resistances. By contrast, tenfold to twentyfold increases in ionic resistances ( $10R_p(t)$  to  $20R_p(t)$ ) may be much less effective in larger cells if the ohmic resistance is sufficiently low and the capacity of lithium-ions initially in the electrolyte within the cathode region is sufficiently large.

The above analyses and understanding should help identify thermal runaway mitigation targets for various safety strategies, and critique their relevance to different stages and timescales of discharge progression. To quickly assess the magnitudes of the ohmic and polarization resistances in higher capacity cells, and to estimate associated joule heating rates experienced upon severe shorting, similar DCIR experiments at high current rates using much shorter pulse durations could be performed to establish a reference for selecting impedance design targets in more dangerous systems. Such analyses offer a pragmatic approach for evaluating and improving LIB safety. These considerations will become critical as advances in LIB chemistry yield higher energy densities and new devices demand a greater degree of system integration, leading to faster temperature accrual and leaving a shorter timeframe to address joule heating.

## 5. Concluding remarks

In this study, the internal resistance and polarization dynamics of lithium-ion batteries in the initial stages of severe short circuit discharge are investigated experimentally, to examine the joule heating regime. Nonlinear resistance, polarization, and joule heating dynamics are identified in direct current internal resistance testing of LIR2450 format LiCoO<sub>2</sub>/graphite 120 mA h coin cells at high current discharge rates. The nature of polarization is clarified using an electrolyte resistance comparison model, indicating rapid depletion of lithium-ions from the electrolyte within the cathode region and consequent temperature accrual are responsible for the nonlinearities. Results are corroborated in external shorting and nail penetration experiments, which reveal a powerful, electrically-controlled, capacitive heating feature immediately upon shorting. Heating is subsequently throttled to lower, ionically-controlled rates as ions quickly transfer to the composite cathode from the electrolyte in the cathode region, leaving the region scarce of ions and relatively resistive.

The prospect of how to address these joule heating features are discussed to support investigation of safe-cell design strategies that take effect in the earliest stages of short circuit discharge. A sensitivity analysis is performed to show how increasing ohmic or polarization resistance would affect the heating rate, as well as their relevance to different timescales. Such analysis could assist in setting impedance exacerbation design targets for cell safety features acting in the joule heating regime. The information gained serves to help bridge the gap in thermal runaway mitigation technological development between primary protection structures and thermally activated failsafe features.

## Acknowledgement

This research is supported by the Advanced Research Projects Agency - Energy (ARPA-E) under Grant No. DE-AR0000396, for which we are grateful to Dr. Ping Liu, Dr. John Lemmon, Dr. Grigori Soloveichik, Dr. Chris Atkinson, and Dr. Dawson Cagle.

## References

- [1] Wang Q, Ping P, Zhao X, Chu G, Sun J, Chen C. Thermal runaway caused fire and explosion of lithium ion battery. *J Power Sources* 2012;208:210–24. <http://dx.doi.org/10.1016/j.jpowsour.2012.02.038>.
- [2] Bandhauer TM, Garimella S, Fuller TF. A critical review of thermal issues in lithium-ion batteries. *J Electrochem Soc* 2011;158:R1. <http://dx.doi.org/10.1149/1.3515880>.
- [3] Lisbona D, Snee T. A review of hazards associated with primary lithium and lithium-ion batteries. *Process Saf Environ Prot* 2011;89:434–42. <http://dx.doi.org/10.1016/j.psep.2011.06.022>.
- [4] Ashtiani C. Analysis of battery safety and hazards' risk mitigation. *ECS Trans* 2008;11:1–11. <http://dx.doi.org/10.1149/1.2897967>.
- [5] Ping P, Wang Q, Huang P, Sun J, Chen C. Thermal behaviour analysis of lithium-ion battery at elevated temperature using deconvolution method. *Appl Energy* 2014;129:261–73. <http://dx.doi.org/10.1016/j.apenergy.2014.04.092>.
- [6] Spontitz R, Franklin J. Abuse behavior of high-power, lithium-ion cells. *J Power Sources* 2003;113:81–100. [http://dx.doi.org/10.1016/S0378-7753\(02\)00488-3](http://dx.doi.org/10.1016/S0378-7753(02)00488-3).
- [7] Ribière P, Grugeon S, Morcrette M, Boyanov S, Laruelle S, Marlair G. Investigation on the fire-induced hazards of Li-ion battery cells by fire calorimetry. *Energy Environ Sci* 2012;5:5271–80. <http://dx.doi.org/10.1039/c1ee02218k>.
- [8] Balakrishnan PG, Ramesh R, Prem Kumar T. Safety mechanisms in lithium-ion batteries. *J Power Sources* 2006;155:401–14. <http://dx.doi.org/10.1016/j.jpowsour.2005.12.002>.
- [9] Doughty DH. Vehicle battery safety roadmap guidance. Albuquerque, NM: National Renewable Energy Laboratory; 2012.
- [10] Lu L, Hua J. A review on the key issues for lithium-ion battery management in electric vehicles. *J Power Sources* 2015;226:272–88. <http://dx.doi.org/10.1016/j.jpowsour.2012.10.060>.
- [11] Xing Y, Ma EWM, Tsui KL, Pecht M. Battery management systems in electric and hybrid vehicles. *Energies* 2011;1840–57. <http://dx.doi.org/10.3390/en4111840>.
- [12] Basu S, Hariharan KS, Mayya S, Song T, Kee D. Coupled electrochemical thermal modelling of a novel Li-ion battery pack thermal management system. *Appl Energy* 2016;181:1–13. <http://dx.doi.org/10.1016/j.apenergy.2016.08.049>.
- [13] Lan C, Xu J, Qiao Y, Ma Y. Thermal management for high power lithium-ion battery by minichannel aluminum tubes. *Appl Therm Eng* 2016;101:284–92. <http://dx.doi.org/10.1016/j.applthermaleng.2016.02.070>.
- [14] Li WQ, Qu ZG, He YL, Tao YB. Experimental study of a passive thermal management system for high-powered lithium ion batteries using porous metal foam saturated with phase change materials. *J Power Sources* 2014;255:9–15. <http://dx.doi.org/10.1016/j.jpowsour.2014.01.006>.
- [15] Remmlinger J, Buchholz M, Meiler M, Bernreuter P, Dietmayer K. State-of-health monitoring of lithium-ion batteries in electric vehicles by on-board internal resistance estimation. *J Power Sources* 2011;196:5357–63. <http://dx.doi.org/10.1016/j.jpowsour.2010.08.035>.
- [16] Zou Y, Hu X, Ma H, Li SE. Combined state of charge and state of health estimation over lithium-ion battery cell cycle lifespan for electric vehicles. *J Power Sources* 2015;273:793–803. <http://dx.doi.org/10.1016/j.jpowsour.2014.09.146>.
- [17] Feng X, Weng C, Ouyang M, Sun J. Online internal short circuit detection for a large format lithium ion battery. *Appl Energy* 2016;161:168–80. <http://dx.doi.org/10.1016/j.apenergy.2015.10.019>.
- [18] Pinnangudi BN, Dalal SB, Medora NK, Arora A, Swart J. Thermal shutdown characteristics of insulating materials used in lithium ion batteries. *Proc. - 2010 IEEE symp prod compliance eng PSES 2010 2010*. p. 4–8. <http://dx.doi.org/10.1109/PSES.2010.5636859>.
- [19] Ji W, Jiang B, Ai F, Yang H, Ai X. Temperature-responsive microspheres-coated separator for thermal shutdown protection of lithium ion batteries. *RSC Adv* 2015;5:172–6. <http://dx.doi.org/10.1039/c4ra11500g>.
- [20] Baginska M, Blaiszik BJ, Merriman RJ, Sottos NR, Moore JS, White SR. Autonomic shutdown of Lithium-ion batteries using thermoresponsive microspheres. *Adv Energy Mater* 2012;2:583–90. <http://dx.doi.org/10.1002/aenm.201100683>.
- [21] Chen Z, Hsu P-C, Lopez J, Li Y, To JWF, Liu N, et al. Fast and reversible thermoresponsive polymer switching materials for safer batteries. *Nat Energy* 2016;1:15009. <http://dx.doi.org/10.1038/NENERGY.2015.9>.
- [22] Feng XM, Ai XP, Yang HX. A positive-temperature-coefficient electrode with thermal cut-off mechanism for use in rechargeable lithium batteries. *Electrochem Commun* 2004;6:1021–4. <http://dx.doi.org/10.1016/j.elecom.2004.07.021>.
- [23] Xia L, Wang D, Yang H, Cao Y, Ai X. An electrolyte additive for thermal shutdown protection of Li-ion batteries. *Electrochem Commun* 2012;25:98–100. <http://dx.doi.org/10.1016/j.elecom.2012.09.038>.
- [24] Cheng CL, Wan CC, Wang YY, Wu MS. Thermal shutdown behavior of PVdF-HFP based polymer electrolytes comprising heat sensitive cross-linkable oligomers. *J Power Sources* 2005;144:238–43. <http://dx.doi.org/10.1016/j.jpowsour.2004.12.043>.
- [25] Zhao R, Zhang S, Gu J, Liu J, Carkner S, Lanoue E. An experimental study of lithium ion battery thermal management using flexible hydrogel films. *J Power Sources*

- 2014;255:29–36. <http://dx.doi.org/10.1016/j.jpowsour.2013.12.138>.
- [26] Kizilel R, Sabbah R, Selman JR, Al-Hallaj S. An alternative cooling system to enhance the safety of Li-ion battery packs. *J Power Sources* 2009;194:1105–12. <http://dx.doi.org/10.1016/j.jpowsour.2009.06.074>.
- [27] Le AV, Wang M, Noelle DJ, Shi Y, Qiao Y. Mitigating thermal runaway of lithium-ion battery by using thermally sensitive polymer blend as cathode binder. *J Appl Polym Sci* 2017;134:45737. <http://dx.doi.org/10.1002/app.45737>.
- [28] Wang M, Le AV, Noelle DJ, Shi Y, Meng YS, Qiao Y. Internal-short-mitigating current collector for lithium-ion battery. *J Power Sources* 2017;348:84–93. <http://dx.doi.org/10.1016/j.jpowsour.2017.03.004>.
- [29] Le AV, Wang M, Shi Y, Noelle DJ, Qiao Y. Heat generation of mechanically abused lithium-ion batteries modified by carbon black micro-particulates. *J Phys D Appl Phys* 2015;48:385501. <http://dx.doi.org/10.1088/0022-3727/48/38/385501>.
- [30] Shi Y, Noelle DJ, Wang M, Le AV, Yoon H, Zhang M, et al. Mitigating thermal runaway of lithium-ion battery through electrolyte displacement. *Appl Phys Lett* 2017;110:63902. <http://dx.doi.org/10.1063/1.4975653>.
- [31] Ding J, Tian T, Meng Q, Guo Z, Li W, Zhang P, et al. Smart multifunctional fluids for lithium ion batteries: enhanced rate performance and intrinsic mechanical protection. *Sci Rep* 2013;3:2485. <http://dx.doi.org/10.1038/srep02485>.
- [32] Zavalis TG, Behm M, Lindbergh G. Investigation of short-circuit scenarios in a lithium-ion battery cell. *J Electrochem Soc* 2012;159:A848. <http://dx.doi.org/10.1149/2.096206jes>.
- [33] Zhao W, Luo G, Wang C-Y. Modeling nail penetration process in large-format Li-ion cells. *J Electrochem Soc* 2015;162:A207–17. <http://dx.doi.org/10.1149/2.1071501jes>.
- [34] Zhao R, Liu J, Gu J. Simulation and experimental study on lithium ion battery short circuit. *Appl Energy* 2016;173:29–39. <http://dx.doi.org/10.1016/j.apenergy.2016.04.016>.
- [35] Santhanagopalan S, Ramadass P, (Zhengming) Zhang J. Analysis of internal short-circuit in a lithium ion cell. *J Power Sources* 2009;194:550–7. <http://dx.doi.org/10.1016/j.jpowsour.2009.05.002>.
- [36] Volck T, Sinz W, Gstrein G, Breitfuss C, Heindl S, Steffan H, et al. Method for determination of the internal short resistance and heat evolution at different mechanical loads of a lithium ion battery cell based on dummy pouch cells. *Batteries* 2016;2:8. <http://dx.doi.org/10.3390/batteries2020008>.
- [37] Park M, Zhang X, Chung M, Less GB, Marie A. A review of conduction phenomena in Li-ion batteries. *J Power Sources* 2010;195:7904–29. <http://dx.doi.org/10.1016/j.jpowsour.2010.06.060>.
- [38] Schönleber M, Uhlmann C, Braun P, Weber A. A consistent derivation of the impedance of a lithium-ion battery electrode and its dependency on the state-of-charge. *Electrochim Acta* 2017;243:250–9. <http://dx.doi.org/10.1016/j.electacta.2017.05.009>.
- [39] Drake SJ, Martin M, Wetz DA, Ostanek JK, Miller SP, Heinzl JM, et al. Heat generation rate measurement in a Li-ion cell at large C-rates through temperature and heat flux measurements. *J Power Sources* 2015;285:266–73. <http://dx.doi.org/10.1016/j.jpowsour.2015.03.008>.
- [40] Cai W, Wang H, Maleki H, Howard J, Lara-Curzio E. Experimental simulation of internal short circuit in Li-ion and Li-ion-polymer cells. *J Power Sources* 2011;196:7779–83. <http://dx.doi.org/10.1016/j.jpowsour.2011.04.024>.
- [41] Lin C, Cui C, Xu X. Lithium-ion battery electro-thermal model and its application in the numerical simulation of short circuit experiment. 2013 World Electr Veh Symp Exhib 2013:1–8. <http://dx.doi.org/10.1109/EVS.2013.6914959>.
- [42] Maleki H, Howard JN. Internal short circuit in Li-ion cells. *J Power Sources* 2009;191:568–74. <http://dx.doi.org/10.1016/j.jpowsour.2009.02.070>.
- [43] Feng X, Lu L, Ouyang M, Li J, He X. A 3D thermal runaway propagation model for a large format lithium ion battery module. *Energy* 2016;115:194–208. <http://dx.doi.org/10.1016/j.energy.2016.08.094>.
- [44] Shearing PR, Darcy E, Keyser M, Tjaden B, Heenan TMM, Jervis R, et al. Characterising thermal runaway within lithium-ion cells by inducing and monitoring internal short circuits. *Energy Environ Sci* 2017;10:1377–88. <http://dx.doi.org/10.1039/C7EE00385D>.
- [45] Waag W, Uwe D. Adaptive estimation of the electromotive force of the lithium-ion battery after current interruption for an accurate state-of-charge and capacity determination. *Appl Energy* 2013;111:416–27. <http://dx.doi.org/10.1016/j.apenergy.2013.05.001>.
- [46] Nejad S, Gladwin DT, Stone DA. Sensitivity of lumped parameter battery models to constituent parallel-RC element parameterisation error. *IECON Proc. (industrial electron conf 40th annua 2014)*. p. 5660–5. <http://dx.doi.org/10.1109/IECON.2014.7049367>.
- [47] Kim JH, Lee SJ, Lee JM, Cho BH. A new direct current internal resistance and state of charge relationship for the li-ion battery pulse power estimation. In: 7th International conf power electron ICPE'07; 2008. p. 1173–8. <https://doi.org/10.1109/ICPE.2007.4692563>.
- [48] Lee S, Kim J, Lee J, Cho BH. State-of-charge and capacity estimation of lithium-ion battery using a new open-circuit voltage versus state-of-charge. *J Power Sources* 2008;185:1367–73. <http://dx.doi.org/10.1016/j.jpowsour.2008.08.103>.
- [49] Dubeshter T, Jorne J. Pulse polarization for Li-ion battery under constant state of charge: part I. Pulse discharge experiments. *J Electrochem Soc* 2017;164:E3539–46. <http://dx.doi.org/10.1149/2.055171jes>.
- [50] Onda K, Ohshima T, Nakayama M, Fukuda K, Araki T. Thermal behavior of small lithium-ion battery during rapid charge and discharge cycles. *J Power Sources* 2006;158:535–42. <http://dx.doi.org/10.1016/j.jpowsour.2005.08.049>.
- [51] Ji Y, Zhang Y, Wang C-Y. Li-ion cell operation at low temperatures. *J Electrochem Soc* 2013;160:A636–49. <http://dx.doi.org/10.1149/2.047304jes>.
- [52] CRC handbook of chemistry and physics. 97th ed. CRC Press; 2006. p. 12.210.
- [53] Valøen LO, Reimers JN. Transport properties of LiPF<sub>6</sub>-based Li-ion battery electrolytes. *J Electrochem Soc* 2005;152:A882. <http://dx.doi.org/10.1149/1.1872737>.
- [54] Porion P, Dougassa YR, Tessier C, El Ouatani L, Jacquemin J, Anouti M. Comparative study on transport properties for LiFAP and LiPF<sub>6</sub> in alkyl-carbonates as electrolytes through conductivity, viscosity and NMR self-diffusion measurements. *Electrochim Acta* 2013;114:95–104. <http://dx.doi.org/10.1016/j.electacta.2013.10.015>.
- [55] Kondo K, Sano M, Hiwara A, Omi T, Fujita M, Kuwae A, et al. Conductivity and solvation of Li<sup>+</sup> ions of LiPF<sub>6</sub> in propylene carbonate solutions. *J Phys Chem B* 2000;104:5040–4. <http://dx.doi.org/10.1021/jp000142f>.
- [56] Lundgren H, Behm M, Lindbergh G. Electrochemical characterization and temperature dependency of mass-transport properties of LiPF<sub>6</sub> in EC:DEC. *J Electrochem Soc* 2014;162:A413–20. <http://dx.doi.org/10.1149/2.0641503jes>.
- [57] Arora P, Doyle M, Godz AS, White RE, Newman J. Comparison between computer simulations and experimental data for high-rate discharges of plastic lithium-ion batteries. *J Power Sources* 2000;88:219–31. [http://dx.doi.org/10.1016/S0378-7753\(99\)00527-3](http://dx.doi.org/10.1016/S0378-7753(99)00527-3).
- [58] Hall DS, Self J, Dahn JR. Dielectric constants for quantum chemistry and Li-ion batteries: solvent blends of ethylene carbonate and ethyl methyl carbonate. *J Phys Chem C* 2015;119:22322–30. <http://dx.doi.org/10.1021/acs.jpcc.5b06022>.